Solar radiation transfer for an ice-covered lake in the central Asian arid climate zone

Cao, Xiaowei

2021

Cao , X , Lu , P , Leppäranta , M , Arvola , L , Huotari , J , Shi , X , Li , G & Li , Z 2021 , ' Solar radiation transfer for an ice-covered lake in the central Asian arid climate zone ' , Inland waters , vol. 11 , no. 1 , pp. 89-103 . https://doi.org/10.1080/20442041.2020.1790274

http://hdl.handle.net/10138/334015
https://doi.org/10.1080/20442041.2020.1790274

acceptedVersion

Transfer of sunlight into an ice-covered lake in the central Asian arid climate zone

Xiaowei Cao[1], Peng Lu[1], Matti Leppäranta[2], Lauri Arvola[3], Jussi Huotari[3], Xiaohong Shi[4], Guoyu Li[5*], Zhijun Li[1*]

[1]State Key Laboratory of Coastal and Offshore Engineering, Dalian University of Technology, Dalian, China

[2]Institute of Atmospheric and Earth Sciences, University of Helsinki, Helsinki, Finland

[3]Faculty of Biological and Environmental Sciences, Ecosystems and Environment Research Programme, Lammi Biological Station, University of Helsinki, Lammi, Finland

[4]Water Conservancy and Civil Engineering College, Inner Mongolia Agricultural University, Hohhot, China

[5]State Key Laboratory of Frozen Soil Engineering, Cold and Arid Regions Environmental and Engineering Research Institute, Chinese Academy of Sciences, Lanzhou, China

Correspondence: Zhijun Li <lizhijun@dlut.edu.cn>

ABSTRACT. Spectral albedo and light transmittance through snow, ice, and water were measured in Lake Wuliangsuhai during the winter of 2016. Data on the weather, the structure of lake ice, and the geochemistry of water were also collected in the 60-day field program. The study lake is very shallow with large wetland area. Compared with polar lakes, solar elevation at the study area is higher and snow accumulation is much lower. Also there is more sediment in the ice. The ice was all congelation ice with a mean thickness of 36.6 cm, and the mean air temperature was –9.6 °C. The broadband albedo and PAR band transmittance were 0.47 and 0.12 (bare ice), 0.79 and 0.04 (new snow), and 0.16 and 0.14 (melting ice), respectively. The level of light allowed for photosynthesis down to the bottom. The ice acted as a grey filter for the sunlight with a mean attenuation coefficient of 2.1 m^{-1}. In water, the attenuation spectra reached a minimum at 563 nm, and weak CDOM absorption at short wavelengths (< 500 nm) as well as weak chlorophyll *a* peak at 660–690 nm were evident. These results expand our knowledge of the evolution of ice and snow cover and their role in the lake ecology in temperate and arid areas.

Keywords: lake ice; snow; irradiance; albedo; transmittance; absorption; time series

Introduction

In the Northern Hemisphere, approximately half the inland surface waters freeze over every year, and the period of ice cover is important in the annual cycle of lakes (Downing et al. 2006; Kirillin et al. 2012). In freshwater lakes, under-ice water temperature varies usually between the freezing point and the temperature of maximum density (4 °C). The vertical stratification shows two main layers, a cold and thin upper layer and a warm lower layer (Leppäranta 2015). Owing to a lack of turbulence in completely ice-covered lakes, even small concentrations of dissolved substances may have a significant influence on stratification fine structure (Kirillin et al. 2012). In the polar and boreal climate zones, the absence or low level of sunlight does not support photosynthesis for several months, and ecosystem respiration largely determines the concentration of dissolved oxygen (Arst et al. 2008; Salonen et al. 2009). This may result in anoxia with harmful side-effects, such as fish kill and the release of phosphorus from the sediment (Wetzel, 2001).

Solar radiation plays a key role in breaking up lake ice by melting at the surface and in the interior, warming under-ice water, and triggering convection cells under ice (Leppäranta et al. 2003, 2019; Kirillin et al. 2012; Salonen et al. 2015; Lu et al. 2018). Water circulation is then closely linked to irradiance beneath the ice because solar radiation is the main force driving dynamics in fully ice-covered lakes (Kirillin et al. 2012). Sediments at the bottom of the lake and strong through flows are also important heat sources. Solar radiation has also a major influence on the chemical and biological processes under the ice (Fang and Stefan, 2009; Jakkila et al. 2009; Pulkkanen and Salonen, 2013).

Investigations of solar radiation have been conducted in boreal lakes (above 50 °N) (Warren 1982; Arst et al. 2006, 2008; Leppäranta et al. 2003, 2010; Lei et al. 2011). These lakes are normally ice-covered for 4–6 months with the maximum ice thickness around 50 cm with 10–20 cm of snow on top. Many studies have also been performed on Arctic sea ice (e.g., Smith and Baker 1981, Grenfell and Maykut 1997, Perovich, 1998; Light et al. 2008; Lu et al. 2018). Although sea ice is optically different from lake ice, the results provide good reference for research on lake ice. But in cold and arid areas at lower latitudes, relatively little is known about the transfer of sunlight through ice into lake water, including the optical properties of ice and the consequent physical and biological conditions under ice.

In cold and arid central Asia, most lakes are frozen in winter down to latitudes of around 35 °N, but only a few studies have been conducted there—for example, in Lake BLH-A (Shi et al. 2014, Huang et al. 2018) and in Nam Co lake (Biermann et al. 2013). Compared with conditions in the boreal zone, the incoming solar radiation is high, and precipitation is low with consequent thin snow cover on ice. These factors strengthen the difference in light conditions between boreal and central Asian lakes in winter. In central Asia, intensive photosynthesis occurs under ice cover throughout the winter, which affects the dissolved oxygen budget (Yang et al. 2016a). These lakes located in the climatological ice margin are especially vulnerable to changes in their annual ice cycle as a result of global warming.

This study is part of a research program on the water quality, physics, and ecology of Lake Wuliangsuhai (40°36'–41°30' N, 108°43'–108°70' E) in Inner Mongolia, China (Song et al. 2019). Lake Wuliangsuhai is a large but very shallow body of water, and nearby deserts can transport fine sand particles onto the ice. Our goal was to measure and analyze the transfer of sunlight through the lake ice to better understand factors controlling the heat budget of the lake (Cao et al. unpublished manuscript), under water physical conditions and water quality, and primary production under ice (Song et al. 2019). In-situ spectral irradiance measurements were performed in winter 2015–2016 ("winter 2016" for short).

Data on the ice cover, snow, and the weather were gathered with manual and automated observations, and the geochemistry of water was mapped based on manually collected samples (Song et al. 2016, 2019). The three primary questions were: (i) How do the optical properties of ice cover, with and without snow, change during winter? (ii) How does under-ice irradiance develop during winter? (iii) Is the level of light sufficient for the growth of primary producers under ice?

Material and methods

The Studied Lake

Lake Wuliangsuhai covers an area of over 300 km^2, and is located in the Inner Mongolian Plateau in Inner Mongolia, China. It is located 1019 m above sea level, and it is 35.4 km long and 6.6 km wide (maximum width 12.7 km). The mean and maximum depths are 1–1.5 m and 2.5–3 m, respectively. The annual mean air temperature is 7.5 °C. The lake is covered with ice on average from early November to the end of March, and the average annual maximum thickness of ice is 63 cm (Yang et al. 2016a). In winter 2016 the measurement site was in the southeastern part of the lake (40° 49.819' N, 108° 45.935' E), where the water depth was 2.2 m and the distance to the shore was about 200 m (Fig. 1). During the field program, from 10 January to 10 March, 2016, solar noon at the site was within 12:45 ± 15 min China Standard Time (CST = UTC + 8 hours), and the solar elevation angle at noon increased monotonically from 28° to 43°.

Observations

The radiation measurements included downward and upward spectral irradiance above the surface, and the downward spectral irradiance spectrum beneath the ice (Table 1). They were carried out in two periods, 12 January to 2 February and 19 February to 4 March. According to the morphology of the ice surface and ice thickness, the observation period was divided into three phases: bare ice (12 January to 4 February), new snow (19 February to 27 February), and the melting (27 February to 5 March). There was nearly no water inflow or outflow in the winter, so the lake water was influenced only by weak winter circulation, sedimentation of suspended particles, and release of impurities during ice growth and melting. These weak variations in water quality were not expected to have much influence on the ice properties (Yang et al. 2016b). Water samples for geochemical analysis were collected on 23 January, and ice samples were collected for crystal structure analysis on 21 January and for ice density analysis on 1 March.

Irradiance. The spectral measurements were performed using three Trios RAMSES-ACC-VIS hyper-spectral radiometers (Rastede, Germany; www.trios.de), and the sampling interval was 10 min. The sensors detected spectral irradiance over a band of 320 to 950 nm, which covers the portion of the solar spectrum that can be transmitted through the layer of ice (Perovich et al. 1993). According to the manufacturer, the sensitivity of the radiometer was 0.04–0.06 mW m^{-2} nm^{-1} in the PAR band. The three radiometers were connected to a TriBox3 unit powered by batteries that were recharged every two days. The set-up of the sensors was based on GFRP (glass fiber-reinforced plastic) and a metal frame (Fig. 2), which was fixed on the ice surface by a metal post. Owing to the relatively thin ice during the installation of the instruments, a block of ice (1 m^2 square) was cut and added as the foundation to fix the metal post (Fig. 2). The downward and upward irradiance sensors were mounted on the tip of a 3-m-long horizontal arm. The vertical distance between the collector of the upward irradiance sensor and the ice surface was 1.35 m. The under-ice downward irradiance sensor was placed 1.75 m below the ice surface. According to the average annual maximum thickness (63 cm), we reserved one meter between the ice and the sensor. This distance was necessary to install and protect the sensor from the bottom of the ice. A shadow in the observation area was caused by the setup itself. The influence of the shadow was about 4‰ as calculated by the method developed by Nicolaus et al. (2010a). Thus, shadow effects were ignored in the data analysis.

Global radiation was measured using two sensors, one for downward and one for upward irradiance (TBQ-2). The measurement band was 300–3000 nm and the accuracy of the sensors was 5% (http://www.jz322.net/prdouct_text.aspx?id=211). The pyranometers were placed 1.5 m above the ice surface, and the data sampling interval was 10 min.

Observations of ice, snow, and weather. Fig. 2 shows the field site. The ultrasonic rangefinder used to record the thickness of ice was 15 m from the spectral irradiance sensor. Ice thickness was also measured by drilling every two days to test the accuracy of the rangefinder. The thickness of snow under the upward irradiance sensor was measured daily after snowfall using a ruler. Its thickness was not uniform in the footprint of the sensor, and the thickness just below the sensor was recorded. Very thin snow cover was observed at the beginning of the campaign, and measurements of snow thickness were commenced only after snowfall on 12 February. Approximately 30 m from the irradiance site, a 6.54-m-high tower was set to monitor air temperature, and wind speed and direction in the surface layer (Li et al. 2009). The cloudiness was measured by daily visual observation at 10:00 during the observation period.

The structure of ice crystals was analyzed from thin sections in a cold laboratory. The ice was columnar-grained, typical of congelation ice, and the grain size was described by the mean diameter (D) of the columns (Durand et al. 2006):

$$D=2\times\sqrt{\frac{1}{n\pi}\sum_{k=1}^{n}A_k} \tag{1}$$

where A_k is the cross-sectional areas of the grains and n is the number of the full ice crystals in the cross-section. The density of ice was calculated by measuring the weight and volume of a cuboid ice sample. The ice sample was cut into a cube of about 10 cm × 10 cm × 5 cm, and each side was measured by an electronic caliper with an accuracy of 0.1 mm. The weight was obtained by an electronic balance with an accuracy of 0.1 g. Then the accuracy of the ice density was 0.4 % or 3.5 kg/m^3. The gas content was calculated by the following formula (Leppäranta, 2015):

$$v_a = 1 - \frac{\rho_i}{\rho_0} \quad (2)$$

where ρ_i is the measured density of the sample and ρ_o = 917 kg m^{-3} is the density of pure ice at 0 °C (Yen, 1981). Temperature correction for density was very small (about 0.2%) and not considered here.

Data processing

The measured irradiance spectra across the 320–950 nm band showed a high noise level at the upper and the lower ends, and thus we limited analyses of the spectra above the ice surface to the band 350–920 nm, as proposed by Nicolaus et al. (2010a). Because radiation passing through ice contains only PAR wavelengths (400–700 nm), only this band was considered for underwater irradiance. Examples of the measured spectra are shown in online supplement (Fig. A-1). Due to problems of accuracy and noise at very low angles of the sun, the daily time window was set to 8:00–18:00 local time (solar noon was close to 12:45), These time limits corresponded to a solar elevation of 10° in the beginning of March.

Spectral irradiance data were interpolated to a 1-nm grid. We denote the downward spectral irradiance above ice by $F_d(\lambda, t)$, the upward spectral irradiance above ice by $F_u(\lambda, t)$ and the downward spectral irradiance in water by $F_w(\lambda, t)$, where λ is wavelength and t is time. The spectral albedo $\alpha = \alpha(\lambda, t)$ and transmittance $\tau = \tau(\lambda, t)$ are

$$\alpha(\lambda,t)=\frac{F_u(\lambda,t)}{F_d(\lambda,t)},\tau(\lambda,t)=\frac{F_w(\lambda,t)}{F_d(\lambda,t)} \quad (3)$$

In order to focus on the internal properties of the ice and water themselves, the absorbance $s(\lambda,t)$ was defined as:

$$s(\lambda,t)=1-\alpha(\lambda,t)-\tau(\lambda,t) \quad (4)$$

The wavelength-integrated albedo, transmittance, and absorption were produced to compare with global radiation measurements and examine PAR transfer for heat balance and photosynthesis under ice. The flux of photons is expressed by the quantum irradiance (Arst et al. 2006):

$$q(t)=\frac{1}{N_a}\int_{PAR}\frac{\lambda}{hc}F\left(\lambda,t\right)d\lambda \quad (5)$$

where N_a is Avogadro's number, h is Planck's constant, c is the velocity of light in vacuum, $F(\lambda, t)$ is irradiance, and PAR index in the integral refers to integration interval (400 nm, 700 nm). The unit usually chosen is μmol m^{-2} s^{-1}. Our measurements provided the planar downward irradiance. According to Arst et al. (2006), the ratio of planar irradiance to scalar irradiance immediately below ice in freshwater lakes is 0.4–0.6.

To obtain spectral irradiance at the bottom of ice, the effect of water between the sensor beneath the ice and the bottom needed to be eliminated. Using the common linear law of attenuation for irradiance and assuming fixed attenuation spectra for ice and water, respectively, $\kappa_i(\lambda, t)$ and $\kappa_w(\lambda, t)$, we have

$$F_w(\lambda) = (1-\alpha)F_d(\lambda)\exp[-\kappa_i(\lambda)h_i - \kappa_w(\lambda)h_w] \quad (5)$$

where h_i is the thickness of ice, and h_w is the distance between the bottom of ice and the underwater sensor. This can be used as a method of inversion to estimate both attenuation spectra from irradiance measurements with at least two (h_i, h_w) combinations (Leppäranta et al. 2010). In phase II, there were only minor changes in the ice thickness and also snow was disturbing factor. In phase III, due to the melting the gas and water content in ice varied, and we could not get a good result to distinct the attenuation between ice and water. In phase I, the ice properties were stable and the ice thickness had the changed significantly. Therefore, the irradiance spectra in phase I was chosen to determine the ice and water attenuation. The average irradiance spectra at 10:00-11:00 hrs on 12 January and 3 February were used, with thicknesses of ice of 33.6 and 40.6 cm, respectively. The result is shown in Fig. 3b. The attenuation spectrum of ice showed a high level for congelation lake ice with a trend of slight decrease toward wavelengths more than 600 nm as observed in a turbid lake (Arst et al. 2008). Ma et al. (2016) reported that the water transparency of Wuliangsuhai was stable in the winter. Therefore, the attenuation coefficient in water is assumed to be constant over the winter. The estimated attenuation of coefficient of ice represents the phases I-II, since the low transmittance in phase II was caused by that presence of snow. For phase III this ice parameter is biased down by up to 50 % than the phase I, but we cannot get more detailed information from the present data.

Results

Weather and ice conditions

The sky was mostly clear during the observation period. There was low cloudiness for 16 days, and only 3 days were fully cloudy (Fig. 4a). The daily noon level of global radiation increased steadily with time from about 500 to 800 W m^{-2} (Fig. 4b). Occasionally, the level dropped down due to snowfall or cloud cover. Albedo was first low over the bare ice surface, and then increased due to snow accumulation. At the beginning of March, the albedo was low again when snow had disappeared and ice had started melting. As is shown in the last sub-section, the albedo had a strong daily cycle with a sharp minimum at noon. Fig. 4c shows that the temperature varied diurnally, and the lowest recorded value was -

24.9 °C at 10:30 hrs on 23 January while the highest (10.2 °C) was measured at 13:20 hrs on 2 March. The mean daily temperature fluctuated between –21.1 °C and 4.2 °C. In the last six days the air temperature decreased from 0.2 to –9.0 °C.

The thickness of ice measured by the ultrasonic sensor and the drilled holes agreed well with each other (Fig. 4d). It steadily increased from 33.8 to 41.1 cm from 10 January to 1 February. It was then stable, and before the middle of February, when the air temperature increased, declined to 35.9 cm. At the end of February, the thickness of ice increased to 38.4 cm for a short time but then rapidly decreased, in 3–10 March, from 30.2 cm to 25.4 cm. A series of photographs of the ice surface at the upward spectral irradiance sensor on different dates are shown in the online supplement (Fig. A-2). Snow was unevenly distributed on the surface mainly due to wind, and irregularities on the ice surface. At the beginning of the campaign, the thickness of snow was not measured because it was less than 0.5 cm, but snowfall occurred on 12 and 18 February (Fig. 4d). After the first snowfall (12 February), the thickness of snow decreased by 1 cm in five days, and after the second, (18 February), it decreased by 4.9 cm in 10 days.

The ice was columnar grained, with crystal size increasing distinctly from top to bottom (Fig. 5). The mean diameter of the cross-section of the ice crystal was 1.2–4.4 cm. The density of ice, measured on 1 March, ranged vertically from 890 to 910 kg m^{-3}. The gas content, estimated from density, varied between 1% and 3 %, which is high for congelation lake ice in winter (Leppäranta et al. 2015).

Geochemistry data on ice and water were collected on 23 January. The detailed results were given in Song et al. (2019). We consider the role of impurities on light transfer here (Table 2): CDOM (colored dissolved organic matter), chlorophyll a, and suspended matter. The estimated CDOM absorption coefficient was 0.002 m^{-1} at 440 nm in ice. The concentration of suspended matter was 175.7 mg/L in water, 3.5 times as much as in ice (49.9 mg/L). The chlorophyll content was 1.14 μg/L in the ice and 0.13 μg/L in the water, their corresponding ratio was about 8.7. This very shallow lake was turbid and eutrophic (Quan et al. 2019, Du et al. 2019), and had very weakly brown color.

Irradiance flux and albedo

Fig. 6 shows daily variations in spectral irradiance and albedo plotted from 8:00 to 18:00 hrs on each day, within ±5 hours from the solar noon. Beyond this period, the solar elevation was lower than 10°.

The daily means around the solar noon were chosen to analyze the spectral data. On days with clear sky, the spectral peak of the mean incident irradiance increased from 546.7 to 774.9 mW m^{-2} nm^{-1}, but the level was reduced by 50% on cloudy days. In phase I, the mean spectral albedo decreased from 0.59 to 0.34 along with a reduction in snow cover. In phase II, due to snowfall, the albedo increased rapidly with a mean and standard deviation of 0.76 ± 0.18, respectively. In the last phase, the albedo quickly decreased from 0.64 to 0.15 because the high temperature caused rapid melting of snow and liquid water appeared on the ice surface.

To get more details of the spectrum, three typical days were selected for further analysis of the irradiance spectra in different phases (Fig. 7): 25 January, 20 February, and 3 March. The incident irradiance gradually increased with time (peak values from 846.1 to 1116.4 mW m^{-2} nm^{-1}), whereas the shapes of the curves did not change much. The maximum incident irradiance occurred at 479 nm and the oxygen absorption peak at 759 nm was clearly visible (Keilin and Hartree, 1949). From 12 to 25 January in phase I, the albedo decreased with the reduction in snow cover on the ice surface (from very thin snow to bare surface), but its spectral distribution was flat. The overall level, however, was largely different. In this phase, the low temperature (average, –10.4 °C) kept the snow dry. Therefore, the thickness, area, and grain structure of snow as well as ambient light conditions affected the albedo. In phase II, the albedo increased to 0.76–0.82 due to snowfall, and an especially large increase was observed in the ultraviolet A band (350–400 nm). In phase III, with an increase in the daily average air temperature from –10.4 to 0.2 °C, and as ice and snow began melting, the spectral albedo dropped sharply to 0.15–0.21 on 3 March.

Fig. 8a shows the results of the broadband. In phase I, the broadband albedo decreased from 0.60 to 0.47 in the presence of no or a very thin layer of snow. After the second snowfall in phase II, the broadband albedo reached 0.79, and in phase III sharply declined from 0.65 to 0.16. The broadband radiation was about 80% of the global radiation. The broadband albedo and albedo from global radiation showed the same temporal evolution, but the former was higher with a mean offset of 0.21 ± 0.12. The PAR albedo had the same temporal evolution as the broadband albedo with an offset of only 0.002 ± 0.003.

Transmittance of light through ice and water

The transmittance of light through ice and water can be determined using the attenuation coefficient in Fig. 3. The results are shown partly in Figs. 6 and 7 together with data on the albedo. In phase I, the mean transmittance increased from 0.067 to 0.120 (ice), and from 0.034 to 0.049 (ice and water) owing to the decreasing snow cover. Snowfall drastically reduced transmittance in phase II, to 0.048 for ice and 0.009 for ice and water. In phase III, the mean transmittance of ice increased from 0.060 to 0.133, and the transmittance from the full ice and water layer to the underwater sensor increased from 0.009 to 0.042 with the melting of ice and snow.

In spectral transmittance (Figs. 7c and e) on three typical days, the maximum occurred at 574 nm for both ice and water. The peak value of transmittance through ice was 0.197 in phase I, decreased to 0.073 in phase II after the snowfall, and increased back to 0.284 during the melting period. The spectral transmittance values of the ice and water layer were only slightly different between phases I and III, at 0.083 and 0.088 respectively. But in phase II, with snowfall, the level sharply reduced to 0.015. For the ice absorbance, the maximum also occurred in phase III, and the average value was 0.67 for ice and 0.77 for ice and water. In phase II, due to the high albedo that caused by the snow cover, the absorbance was the lowest of the three phases, and the average value was 0.16 (ice) and 0.20 (ice and water). In phase I, the average absorbance was 0.44 and 0.49 respectively.

Fig. 8b shows the distribution of the incident PAR for the albedo, absorption, and transmittance of ice. In phase I, absorption ranged from 0.34 to 0.54, and transmittance was 0.07–0.12. In phase II, the mean absorption and transmittance decreased to 0.19 and 0.04, respectively, due to snow cover. In the last phase, PAR absorption quickly increased to 0.70 because of the increased liquid water content of ice. The transmittance increased little from 0.06 to 0.14. Overall, the transmittance did not vary much, and the main variation was in the balance between absorption and reflectance.

Spectral irradiance was transformed to PAR quantum irradiance using Eq. (4). The downward quantum PAR irradiance was 113.9 ± 89.4 μmol m^{-2} s^{-1} at the bottom of the ice and 21.8 ± 17.4 μmol m^{-2} s^{-1} at the underwater sensor in phase I. After the snowfall in phase II, it decreased to 30.2 ± 16.9 μmol m^{-2} s^{-1} (ice bottom) and 6.5 ± 3.6 μmol m^{-2} s^{-1} (underwater sensor), and, in phase III increased back to 183.2 ± 113.4 μmol m^{-2} s^{-1} (ice bottom) and 34.7 ± 20.2 μmol m^{-2} s^{-1} (underwater sensor). In the water below ice, the estimated scalar quantum irradiance was twice the downward planar irradiance (Arst et al. 2006).

In phases I and III, the level of light was more than 20 μmol m^{-2} s^{-1} at the lake bottom

(0.5 m from the underwater sensor) around solar noon. This represents the level of irradiance usually considered sufficient for primary production, expressed as euphotic depth equal to 1 % of the incident irradiance (Reynolds et al. 2006). Indeed, growing macro fauna were observed at the bottom. But in phase II, primary production was limited. The ratio of the PAR quantum irradiance to irradiance power was approximately 4.6 μmol J^{-1} in air, as follows from the direct integration of Eq. (5) because sunlight is nearly white in the PAR band. The spectrum of light was modified in its transmission through ice and water, and, consequently, the ratio changed to range from 4.6 to 4.8 μmol J^{-1} at the underwater sensor. For comparison, Reinart et al. (1998) found ratios between 4.8–5.5 μmol J^{-1} in a large set of lakes in north Europe. Downward irradiance reaching the bottom of the lake was evaluated using the estimated attenuation coefficients of water. It was on average 12.7 μmol m^{-2} s^{-1}, and ranged from 3.3 to 25.9 μmol m^{-2} s^{-1}.

Daily cycle of light transfer

The daily cycle is important for Lake Wuliangsuhai because the solar elevation reached 30–42° at noon during the winter and the sky was mostly clear, thus rendering considerably the contributions of direct solar radiation to the melting of ice. By comparison, the solar elevation is 10–25° less in boreal lakes.

The daily cycle of the spectral downward irradiance, albedo, transmittance, and absorption on March 2 are shown in Fig. 9. The albedo was higher in the morning than in the afternoon. There are two main reasons for this phenomenon. First, the high solar elevation led to greater solar radiation on the surface of ice at noon and, second, the high level of radiation and sediments on the ice surface caused melting that produced liquid water in the surface layer. The increase in the content of liquid water reduced the albedo. At nighttime, the ice and snow surface froze again, causing a high albedo in the morning. This is different from lake ice at high latitude and sea ice in the Arctic. Leppäranta et al. (2010) measured the albedo in Lake Vendysrskoe (62^{o} 10'–20' N) during the melting period, and found that the albedo was the minimum at solar noon, and maximum in the morning and evening. The albedo of Arctic sea ice was observed to be nearly unchanged during a polar day in summer by Lei et al. (2010).

Actually, in all phases there was an obvious and similar diurnal behavior with maximum in the morning and minimum in the evening. In phases II and III the air temperature was close to or above zero to create moisture enough to put the albedo down. In phase I, the diurnal behavior was not obvious as that in phase II and III. It was mainly caused by the low air temperature, stable ice properties and a local effect along with the sun's azimuth angle. The daily cycle of the spectral albedo in three phases is shown in the online supplement (Fig. A-3)

Transmittance and absorption were higher at noon and in the afternoon than in the morning (Figs. 9c, d), and this trend was opposite to that of the albedo. The mean transmittance and absorption were 0.084 and 0.441, respectively, at 8:00. They were close at 13:00 and 18:00 hrs, with transmittance values of 0.121 and 0.129 and absorption values of 0.610 and 0.642, respectively. Transmittance peaked at approximately 550 nm and was skewed toward longer wavelengths.

Fig. 10 shows the daily cycle of the downward, upward, and transmitted PAR irradiance in phase III. The maximum downward and transmitted irradiance occurred at 13:00, with values of 300.79 and 36.80 W m^{-2}, respectively. The upward PAR irradiance peaked slightly earlier at about 11:30, and the irradiance was 87.58 W m^{-2}. The earlier occurrence was caused by surface melting that increased surface water content and reduced the albedo.

Discussion

Albedo and transmittance

Compared with high-latitude boreal and tundra lakes, Lake Wuliangsuhai has a shorter ice season and limited accumulation of snow owing to its low latitude and arid climate. Fig. 11 shows a comparison of the spectral albedo and transmittance of lake ice for two lakes in Finland at 61° N (Lei et al. 2011), and observations of Arctic sea ice at different stages of melting (Nicolaus et al. 2010b). The snow and ice conditions at these sites are summarized on the online appendix Table 1.

The shapes of the spectral albedo in the three phases of Lake Wuliangsuhai were similar to those of the two Finnish lakes. For the bare ice period (phase I), the maximum albedo was 0.26 in Iso Valkjärvi and 0.51 in Wuliangsuhai. This difference was caused by the thin snow cover in Wuliangsuhai and the fine granular ice in the top layer of Iso Valkjärvi (Lei et al. 2011). In the presence of snow cover (phase II), the maximum albedo was high in both lakes (0.76 for Iso Valkjärvi and 0.82 for Wuliangsuhai). During the melting period (phase III), the maximum albedo decreased to 0.20 in both Wuliangsuhai and Vesijärvi. The same value was due to a thin layer of water on the ice surface. The maximum value of lake ice transmittance was 0.41 (Iso Valkjärvi) and 0.20 (Wuliangsuhai) during the bare ice period (phase I). This difference was also caused by the thin snow cover on Wuliangsuhai. The snow cover (phase II) caused low ice transmittance (0.02 Iso Valkjärvi for and 0.07 for Wuliangsuhai). During phase III, the maximum transmittance increased in both lakes, to 0.41 in Vesijärvi and 0.28 in Wuliangsuhai. From the shapes of the curves of spectral transmittance, Vesijärvi had higher transmittance at 400–550 nm than at 550–700 nm, but the maximum transmittance occurred at 500–600 nm in Wuliangsuhai. This was possibly caused by sediment on the ice surface in Lake Wuliangsuhai.

Compared with Wuliangsuhai, the albedo and transmittance of sea ice were very different. The maximum albedo was higher than that for Wualiangsuhai in the three phases, especially for the bare ice and melting periods. In phase I, this difference was caused by the snow–ice in the surface layer of sea ice (Nicolaus et al. 2010b). In phase III, this occurred because there was no melt ponds at the sea ice site (Nicolaus et al. 2010b), but a thin layer of water was present in Wuliangsuhai. The transmittance of sea ice was low in the three phases (0.071, 0.003, and 0.117). There are two reasons: the difference in the physical properties of ice and ice thickness, which was six times higher at the sea ice site (Table 5).

Attenuation coefficients

The light attenuation spectrum of dry ice had large uncertainties at the ultraviolet and infrared boundaries owing to the low level of signals in underwater data (Fig. 3). The spectral curve sloped down toward longer wavelengths across the PAR band, likely owing to the suspended matter. The CDOM level was low in ice but the concentration of suspended matter was high (Table 2). There was no sign of the chlorophyll *a* peak in ice transmittance, as expected owing to its low level, while this peak was evident in water.

The estimated light attenuation spectrum of water is also shown in Fig. 3. It was identical in magnitude to light attenuation in ice. This high level likely occurred owing to the high concentration of suspended matter (Table 2). The chlorophyll *a* signal was also observed in the spectrum. Fig. 10 shows the decomposition of the attenuation curve due to the effects of pure water and optically active substances. Pure water had a significant impact only in the red and near-infrared bands, whereas CDOM was important at wavelengths smaller than 500 nm. For CDOM, normal exponentially decreasing absorption with wavelength was assumed. The difference between the measured spectrum and the "pure water + CDOM" curve was mostly due to suspended matter, which exhibited attenuation due to absorption and scattering from 2 m^{-1} to 1 m^{-1} across the PAR band (see, e.g., Arst et al. 2008). Overall, the spectrum shows that this is a turbid lake with low levels of CDOM (or low level of color), and has high primary production under ice.

Data quality

Previous studies (e.g., Nicolaus et al. 2010a; Lei et al. 2012) have shown that the Trios instruments applied in this study for the measurement of spectral irradiance are suitable for long–term installation in cold regions. The impact of the setup used in our measurements was estimated to be smaller than 0.5%, and smaller than the setup used by Nicolaus et al. (2010a) in the Arctic, where they had a 2.8%–7.7% downward bias in the measured spectral upward irradiance. Another problem in our setup was that snow accumulated around the instrument platform due to wind. The mean offset of the broadband albedo and albedo from global radiation was 0.21 ± 0.12. Nicolaus et al. (2010b) also reported this value for Arctic sea ice, but their offset was 0.11 ± 0.05. The difference is likely owing to local variations in the ice surface and snow cover at our site (Fig. 2).

We used the arm under ice to fix the sensor for underwater measurement, like Mobley et al. (1998), and Light et al. (2008). The arm significantly reduced the influence of shadowing. However, to protect the sensor, a one-meter distance between the bottom of the ice and the underwater sensor was required. To separate light transfer in ice from that in water, an inversion method was employed. The results provide a representative attenuation spectrum for ice and water, but this separation did not provide time-dependent information for the two attenuation spectra. These spectra were used to estimate the amount of light just beneath the ice, and the total attenuation of ice and the layer of water from the bottom of ice to the sensor was based on measurements. The attenuation spectrum of water depended on the quality of water and incident irradiance. There are no prior measurements of light transfer in Wuliangsuhai Lake to compare ours with. In future measurements, the problem should be solved by reducing the distance between the sensor and the bottom of the ice and adding another sensor in the water.

Another factor affecting the underwater measurements was the growth of algae and accumulation of sediments on the optical sensors. We did not clean the underwater sensor during the observation period because previous experience in the lake revealed that there were no obvious sediments on the sensor after picking it up, and significant impact on the ice surface properties cannot be avoided with breaking the ice layer during the data collection. An idealized solution to this issue is an automated cleaning operation together with an underwater online camera, and it is under consideration for our investigations in future.

Conclusions

In this study, a field investigation of the transfer of sunlight through lake ice was conducted in Lake Wuliangsuhai, Inner Mongolia, in the winter of 2016. This lake in the central Asian arid climate zone is different from boreal and polar lakes. The measurements consisted of observations of the weather and ice conditions, spectral irradiance, and the geochemistry of ice and water. The purpose was to examine the evolution of the spectral albedo and the transmittance of lake ice during the winter, and primary production in the water body of the lake.

The results revealed that the albedo and transmittance of lake ice were mainly affected by surface conditions, such as snow and water. The broadband albedo and PAR band transmittance were in three phases as follows: 0.47 and 0.12 (bare ice), 0.79 and 0.04 (new snow), and 0.16 and 0.14 (melting period). The estimated planar quantum irradiance reaching the bottom of the lake was approximate 12.7 $\mu mol\ m^{-2}\ s^{-1}$, which is sufficient for primary production. The solar elevation and sediment on the surface of ice caused daily variation in the albedo and transmittance of lake ice. The estimated light attenuation spectrum showed that the lake is a turbid lake with a low level of CDOM.

In this first step of a research program on the ecological state of Wuliangsuhai Lake, we now understand how sunlight is transmitted through ice and water in this lake. We collected more comprehensive data at Wuliangsuhai in subsequent winters. In future analysis, these data will be employed to assess models of radiation transfer and analyze the mass balance of frozen lakes in the central Asian arid climate zone. The results can also help examine the use of high-resolution optical satellite data for the remote sensing of ice-covered lakes. The findings in this study together with knowledge from previous measurements of boreal lakes will improve our understanding of the response of ice-covered lakes to global changes in climate.

Acknowledgments

This research was supported by the National Major Research High Resolution Sea Ice Model Development Program of China (2018YFA0605901), and the National Natural Science Foundation of China (51579028, 41922045, 41876213). Matti Leppäranta, Lauri Arvola (298312, 310997, 315527, 325382) and Jussi Huotari (311520, 316866, 325446) were supported by the Bilateral Exchange Programme of the Chinese Academy of Sciences and Academy of Finland. Xiaowei Cao was supported by China Science & Technology Association's Excellent Chinese and Foreign Youth Exchange Program (2017).

References

Arst H., Erm A., Leppäranta M. and Reinart A. 2006. Radiative characteristics of icecovered fresh- and brackish-water bodies. P. Est. Acad. Sci. **55**: 3-23.

Arst H., Erm, A., Herlevi, A,. Kutser T., Leppäranta M., Reinart A. and Virta J. 2008. Optical properties of boreal lake waters in Finland and Estonia. Boreal Environ. Res. **13**: 133–158.

Biermann, T., Babel, W., Ma W., Chen X., Thiem E., Ma Y. and Foken T. 2014. Turbulent flux observations and modelling over a shallow lake and a wet grassland in the Nam Co basin, Tibetan Plateau. Theor. Appl. Climatol. **116**: 301-316. doi: 10.1007/s00704-013-0953-6

Downing J. A., Duarte C. M., Tranvik L. J., Striegl R. G., Mcdowell W. H., Kortelainen P., Caraco N. F., Melack J. M. and Middelbing J. J. 2006. The global abundance and size distribution of lakes, ponds, and impoundments. Limnol. Oceanogr. **51**: 2388-2397. doi: 10.4319/lo.2006.51.5.2388.

Du D., Li C., Shi X., Zhao S., Quan D. and Yang Z. Seasonal changes of nutritional status of lake Wuliangsuhai. J. Arid Land Resour. Environ. **33(12)**: 187-192 (In Chinses). doi: 10.13448/j.cnki.jalre.2019.365

Durand, G., Gagliardini, O., Thorsteinsson, T., Svensson, A., Kipfstuhl, S. and Dahl-Jensen, D. 2006. Ice microstructure and fabric: an up-to-date approach for measuring textures. J. Glaciol. **52**: 619-630. doi: 10.3189/172756506781828377

Fang X. and Stefan H. G. 2009. Simulations of climate effects on water temperature, dissolved oxygen, and ice and snow covers in lakes of the contiguous United States under past and future climate scenarios. Limnol. Oceanogr. **54**: 2359-2370. doi: 10.4319/lo.2009.54.6_part_2.2359

Grenfell T. C. and Maykut G. A. 1977. The optical properties of ice and snow in the arctic basin. J. Glaciol. **18**: 445-463. doi: 10.3189/S0022143000021122

Huang W. F., Cheng B., Zhang J., Zhang Z., Vihma, T., Li Z. and Niu F. 2019. Modeling experiments on seasonal lake ice mass and energy balance in the Qinghai–Tibet Plateau: A case study. Hydrol. Earth Syst. Sci. Dicuss. 23: 2173-2186. doi: 10.5194/hess-23-2173-2019

Jakkila J., Leppäranta M., Kawamura T., Shirasawa K. and Salonen K. 2009. Radiation transfer and heat budget during the ice season in Lake Pääjärvi, Finland. Aquat. Ecol. **43**: 681-692. doi: 10.1007/s10452-009-9275-2

Kirillin G., Leppäranta M., Terzhevik A., Bernhardt .J, Engelhardt C., Granin N., Golosov S., Efremova T., Palshin N., Sherstyankin P., Zdorovennova G. and Zdorovennov R. 2012. Physics of seasonally ice-covered lakes: major drivers and temporal/spatial scales. Aquat. Ecol. **74**: 659–682. doi: 10.1007/s00027-012-0279-y

Keilin D. and Hartree E. F. 1949. Effect of low temperature on the absorption spectra of haemoproteins; with observations on the absorption spectrum of oxygen. Nature **164**: 254. doi: 10.1038/164254a0

Lei R. B., Leppäranta M., Erm A., Jaatinen E. and Pärn O. 2010. Field investigations of apparent optical properties of ice cover in Finnish and Estonian lakes in winter 2009. Est. J. Earth Sci. **60:** 50-64. doi: 10.3176/earth.2011.1.05

Lei R. B., Zhang Z. H., Matero I., Cheng B., Li Q., and Huang, W. F. 2012. Reflection and transmission of irradiance by snow and sea ice in the central Arctic Ocean in summer 2010. Polar Res. **31**: 31. doi: 10.3402/polar.v31i0.17325

Leppäranta M. 2015. Freezing of lakes and the evolution of their ice cover. Springer-Praxis, Heidelberg. doi: 10.1007/978-3-642-29081-7(2015)

Leppäranta M., Reinart A., Erm A., Arst H., Hussainov M. and Sipelgas L. 2003. Investigation of ice and water properties and under-ice light fields in fresh and brackish water bodies. Nord. Hydrol. **34**(3): 245-266. doi: 10.1023/A:1021142404009

Leppäranta M., Terzhevik A. and Shirasawa K. 2010. Solar radiation and ice melting in Lake Vendyurskoe, Russian Karelia. Hydrol. Res. **41**: 50-62. doi: 10.2166/nh.2010.122

Leppäranta M., Heini A., Jaatinen E. and Arvola L. 2012. The influence of ice season on the physical and ecological conditions in Lake VanaJanselkä, southern Finland. Water Qual. Res. J. of Canada **47**: 287–299. doi: 10.2166/wqrjc.2012.003

Leppäranta M., Lindgren E., Wen L., Kirillin G. 2019. Ice cover decay and heat balance in Lake Kilpisjärvi in Arctic tundra. J. Limnol. doi: 10.4081/jlimnol.2019.1879

Li Z. J., Yang Y., Peng X. M., Wang G. Z. and Lu Y. C. 2009. The analysis of the field observation data of fresh ice growing process in Hongqipao Reservoir of Heilongjiang. J. Xi'an Univ. Technol. **25**:270-274 (in Chinese). doi: 10.3969/j.issn.1006-4710.2009.03.004

Light B., Grenfell T. C. and Perovich D. K. 2008. Transmission and absorption of solar radiation by arctic sea ice during the melt season. J. Geophys. Res. Oceans **113**. doi: 10.1029/2006JC003977

Lu P., Cao X. W., Wang Q. K., Leppäranta M. and Cheng B. 2018. Impact of a Surface Ice Lid on the Optical Properties of Melt Ponds. J. Geophys. Res. Oceans **123**: 8313-8328. doi: 10.1029/2018JC014161

Ma H., Li C. Y., Zhao S. N. and Zhou X. X. 2016. Spatial-temporal distribution of water transparency and its relationships with environmental factors in Wuiangsu Lake, Inner Mongolia. Bull. Soil Water Conserv. **36(5)**: 273-277 (In Chinese). doi: 10.13961/j.cnki.stbctb.2016.05.050

Mobley C. D., Cota G. F., Grenfell T. C., Maffione R. A., Pegau W. S. and Perovich D. K. 2002. Modeling light propagation in sea ice. IEEE T. Geosci. Remote **36**: 1743-1749. doi: 10.1109/36.718642

Nicolaus M., and Hudson S. R. 2010a. A modern concept for autonomous and continuous measurements of spectral albedo and transmittance of sea ice. Cold Reg. Sci. Technol.

62: 14-28. doi: 10.1016/j.coldregions.2010.03.001

Nicolaus M., Gerland S., Hudson S.R., Hanson S., Haapala J. and Perovich D. K. 2010b. Seasonality of spectral albedo and transmittance as observed in the arctic transpolar drift in 2007. J. Geophys. Res. Oceans **115**. doi: 10.1029/2009JC006074

Perovich D. K., Cota G. F., Maykut G. A. and Grenfell T. C. 1993. Bio-optical observations of first-year arctic sea ice. Geophys. Res. Lett. **20**: 1059–1062. doi: 10.1029/93GL01316

Perovich D. K., Jones K. F., Light B., Eicken H., Markus T., Stroeve J. and Lindsay R. 2011. Solar partitioning in a changing arctic sea-ice cover. Ann. Glaciol. **52**： 7. doi: 10.3189/172756411795931543

Pulkkanen M. and Salonen K. 2013. Accumulation of low-oxygen water in deep waters of ice-covered lakes cooled below 4 °C. Inland Waters **3**： 15-24. doi: 10.5268/IW-3.1.514

Quan D., Shi X., Zhao S., Zhang S. and Liu J. Eutrophication of Lake Ulansuhai in 2006 — 2017 and its main impact factors. J. Lake Sci. **31(5)**: 1259-1267. doi: 10.18307/2019.0503

Reinart A, Arst H, Blanco-Sequeiros A and Herlevi A 1998. Relation between underwater irradiance and quantum irradiance in dependence on water transparency at different depths in the water bodies. J. Geophys. Res. **103**： 7749–7752. doi:

10.1029/97jc03645

Reynolds, C. 2006. Ecology of phytoplankton. Cambridge University Press, Cambridge.

Salonen K., LeppäRanta M., Viljanen M., and Gulati R. D. 2009. Perspectives in winter limnology: closing the annual cycle of freezing lakes. Aquat. Ecol. **43(3)**: 609-616. doi: 10.1007/s10452-009-9278-z

Salonen K., Pulkkanen M., Salmi P. and Griffiths R. 2015. Interannual variability of circulation under spring ice in a boreal lake. Limnol. Oceanogr. **59**: 2121-2132. doi: 10.4319/lo.2014.59.6.2121

Shi L., Li Z. J., Niu F., Huang W. F., Lu P., Feng, E., and Han H. W. 2014. Thermal diffusivity of thermokarst lake ice in the beiluhe basin of the qinghai–tibetan plateau. Ann. Glaciol. **55**: 153-158. doi: 10.3189/2014AoG66A192

Smith R. C. and Baker K. S. 1981. Optical properties of the clearest natural waters (200–800 nm). Appl. Optics **20**: 177–184. doi: 10.1364/ao.20.000177

Song S., Jia K. L., Shi X. H., Hu H., Zhao S. N. and Wu Y. 2016. The water quality variation characteristics of Wulansuhai lake in freezing thawing process. J. Arid Land Resour. Environ. **30**: 113-118 (In Chinese). doi: 10.13448/j.cnki.jalre.2016.020

Song S., Li C., Shi X., Zhao S., Li Z., Bai Y., Cao X., Wang Q., Huotari J., Tulonen T., Uusheimo S., Leppäranta M. and Arvola L. 2019. Under-ice metabolism in a shallow lake (Wuliangsuhai) in Inner Mongolia, in cold and arid climate zone. Freshwater

Biology. 64(10): 1710-1720. doi: 10.1111/fwb.13363

Warren, S. G. 1982. Optical properties of snow. Rev. Geophys. Space Phys. 20: 67:89.

Wetzel R. G. 2001. Limnology: Lake and River Ecosystems, 3rd ed., Academic Press, San Diego.

Tschudi M. A., Maslanik J. A. and Perovich D. K. 2008. Derivation of melt pond coverage on arctic sea ice using modis observations. Remote Sens. Environ. **112**： 2605-2614. doi: 10.1016/j.rse.2007.12.009

Yang F., Li C. Y., Shi X. H., Zhao S. N. and Hao Y. Z. 2016a. Impact of seasonal ice structure characteristics on ice cover impurity distributions in Lake Ulansuhai. J. Lake Sci. **28**: 455-462 (In Chinese). doi: 10.18307/2016.0226

Yang F., Li C. Y., Leppäranta M., Shi X. H., Zhao S. N. and Zhang C. F. 2016b. Notable increases in nutrient concentrations in a shallow lake during seasonal ice growth. Water Sci. Technol. **74**: 2773-2783. doi: 10.2166/wst.2016.433

Yen, Y. C. 1981. Review of thermal properties of snow, ice, and sea ice. Crrel Rep, 27.

Figure legends

Fig. 1. Location of Lake Wuliangsuhai, Inner Mongolia, the field site in winter 2016 marked by red star.

Fig. 2. Position of equipment (date 27 January 2016) and schematic diagram of the set-up of the three RAMSES sensors.

Fig. 3. The ice + water attenuation spectra in three phases (at 11:00 on 12 January, 19 and 27 February), and the estimated attenuation spectra of ice and water in phase I.

Fig. 4. (a) Cloudiness, (b) Global radiation and albedo at noon (13:00), (c) Air temperature and the mean daily air temperature during the observation period, and (d) Ice and snow thickness.

Fig. 5. (a) Vertical ice crystal structure under polarized light (left) and ice sample under normal light (right), (b) profile of the mean diameter of ice crystals in the horizontal plane and (c) profile of ice density and gas content.

Fig. 6. Time series of (a) incident solar irradiance, (b) albedo, (c) transmittance of lake ice, (d) transmittance of ice and a water layer beneath ice, and (e) cloudiness in tenths. The spectrum is shown for 8:00–18:00 each day. The white areas are missing data due to malfunction of Tribox3.

Fig. 7. The spectral results for three typical days in different phase at solar noon: 25 January (solar elevation SE = 30.3º), 20 February (SE = 38.3°), and 3 March (SE = 42.4º). (a) Incident solar irradiance, (b) Albedo, (c) Transmittance of ice, (d) Absorbance of ice,

(e) Transmittance of ice and water, and (f) Absorbance of ice and water.

Fig. 8. (a) Broadband and PAR albedo. (b) PAR albedo and absorption and transmittance relative to the incident PAR irradiance.

Fig. 9. Incident irradiance, albedo, transmittance and absorption of different hrs at 8, 10, 13, 15 and 18 hrs on 2 March. At the end points the solar elevation was about 10°. At 20 and 4 hrs and between the incident irradiance was zero.

Fig. 10. Daily cycle of downward, upward and transmitted PAR irradiance on 2 March.

Fig. 11. The spectral albedo and transmittance of ice in lakes Wuliangsuhai, Iso Valkjärvi and Vesijärvi (Lei et al. 2011), and Arctic (Nicolaus et al. 2010b) in different phases (blue for phase I, black for phase II, and red for phase III).

Fig. 12. Decomposition of light attenuation spectra for Lake Wuliangsuhai. Pure water shows standard pure water absorption curve (Smith and Baker, 1981), and CDOM was added based on the observed value of 0.004 m–1 (at 440 nm).

Fig. A-1. The incident (left) and transmitted (right) solar irradiance on 12 January. The lines show the limits of the band taken for the analyses (broadband, 350–920 nm, and PAR, 400–700 nm).

Fig. A-2. Ice surface conditions under the downward irradiance sensor (in the red square) on different dates in winter 2016.

Fig. A-3. The diurnal cycle of the albedo in three phases and the solar noon was about

13:00.

Tables

Table 1. Solar radiation and complementary measurements at Lake Wuliangsuhai in winter 2016. Manual visual observations were recorded daily, and recordings by the instruments were continuous.

Quantity	Sensor (manufacturer)	Range	Accuracy	Time
Spectral irradiance	Trios (Rastede, Germany)	320–950 nm band (3 nm resolution)	±3%	12 Jan to 2 Feb and 19 Feb to 4 Mar
Global radiation	TBQ-2 (JST, China)	300–3000 nm band	±5%	
Ice thickness (ultrasonic)	WUUL-I (WHU, China)	10–200 cm	±0.2 cm	
Air temperature	PTS-3 (JST, China)	–40–+80 °C	±0.04 °C	10 Jan to 10 Mar
Wind speed	PC-2FB (JST, China)	0.1-30 m/s	±0.4 m/s	
Wind direction	EC-9X1A (JST, China)	0-360°	±0.6 °	
Cloudiness	Visual	0-10/10	±2/10	Every day at 10:00 am.

Table 2. Geochemistry data of ice and water measured on 23 Jan, 2016. CDOM was not measured in winter 2016 but estimated from values of subsequent winter, assuming the same ice/water ratio for CDOM as for nutrients in 2016 (total nitrogen and phosphorus).

Quantity	Ice	Water	Ice/water ratio
Suspended matter（mg/L）	49.9	175.7	0.28
Chlorophyll-*a*（μg/L）	0.14	1.13	0.12
Total nitrogen（mg/L）	0.37	0.70	0.53
Total phosphorus（mg/L）	0.032	0.064	0.50
CDOM（m^{-1}）, at 440 nm	(0.002)	(0.004)	(0.5)

Table 3. Statistics of broadband (BB, 320–950 nm) and PAR (400–700 nm) irradiance fluxes, albedo, transmittance at solar noon, and ratio *q/F* of quantum irradiance to irradiance power in water from spectral radiometers in winter 2016. Irradiance power in W m^{-2}, quanta in μmol $m^{-2}s^{-1}$.

	Maximum		Minimum		Mean	SD
Incident (BB)	470.0	(01 Mar)	163.1	(20 Feb)	357.5	89.4
Incident (PAR)	300.2	(01 Mar)	105.8	(20 Feb)	229.9	57.5
Albedo (BB)	0.80	(20 Feb)	0.15	(05 Mar)	0.56	0.17
Albedo (PAR)	0.80	(20 Feb)	0.16	(05 Mar)	0.55	0.16
Absorption by ice PAR	0.70	(05 Mar)	0.17	(20 Feb)	0.36	0.14
Ice transmittance (PAR)	0.14	(05 Mar)	0.04	(20 Feb)	0.08	0.03
Ice and water transmittance (PAR)	0.04	(28 Jan)	0.01	(20 Feb)	0.03	0.01
Quantum irradiance just below ice	295.9	(05 Mar)	32.1	(19 Feb)	142.6	85.9
Quantum irradiance 1.35 m below ice	55.0	(05 Mar)	6.9	(19 Feb)	27.5	15.9
q/F	4.68	05 Mar	4.62	20 Feb	4.64	0.02

Figures

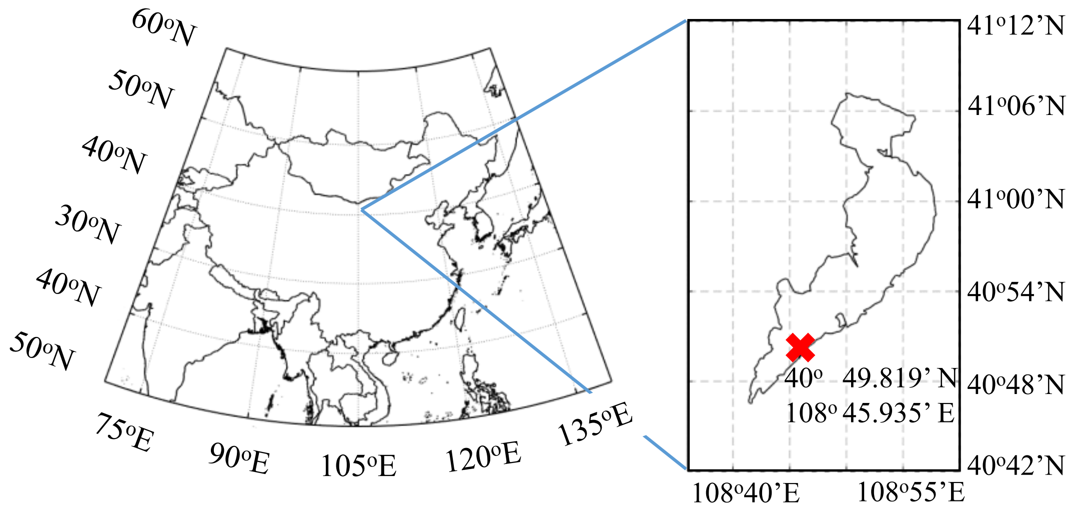

Fig. 1. Location of Lake Wuliangsuhai, Inner Mongolia, the field site in winter 2016 marked by red star.

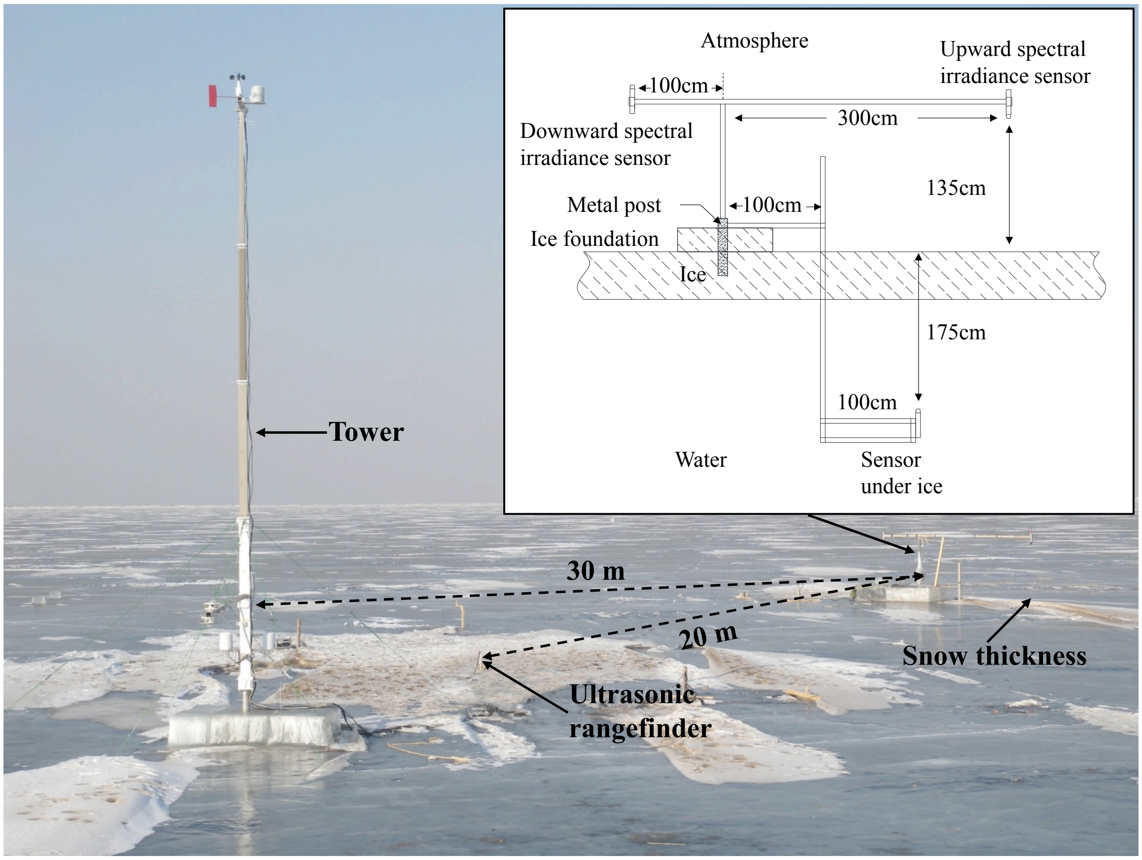

Fig. 2. Position of equipment (date 27 January 2016) and schematic diagram of the set-up of the three RAMSES sensors.

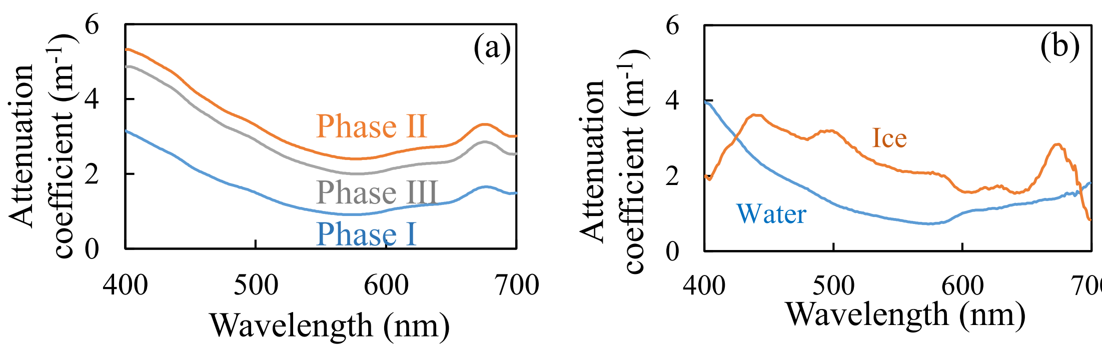

Fig. 3. The ice + water attenuation spectra in three phases (at 11:00 on 12 January, 19 and 27 February) (a), and the estimated attenuation spectra of ice and water in phase I (b).

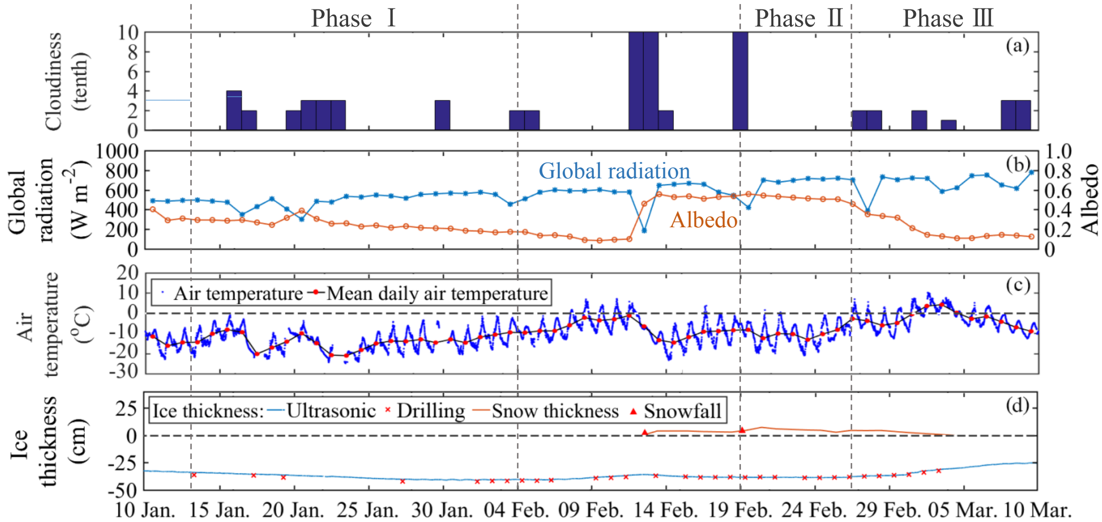

Fig. 4. (a) Cloudiness, (b) Global radiation and albedo at noon (13:00), (c) Air temperature and the mean daily air temperature during the observation period, and (d) Ice and snow thickness.

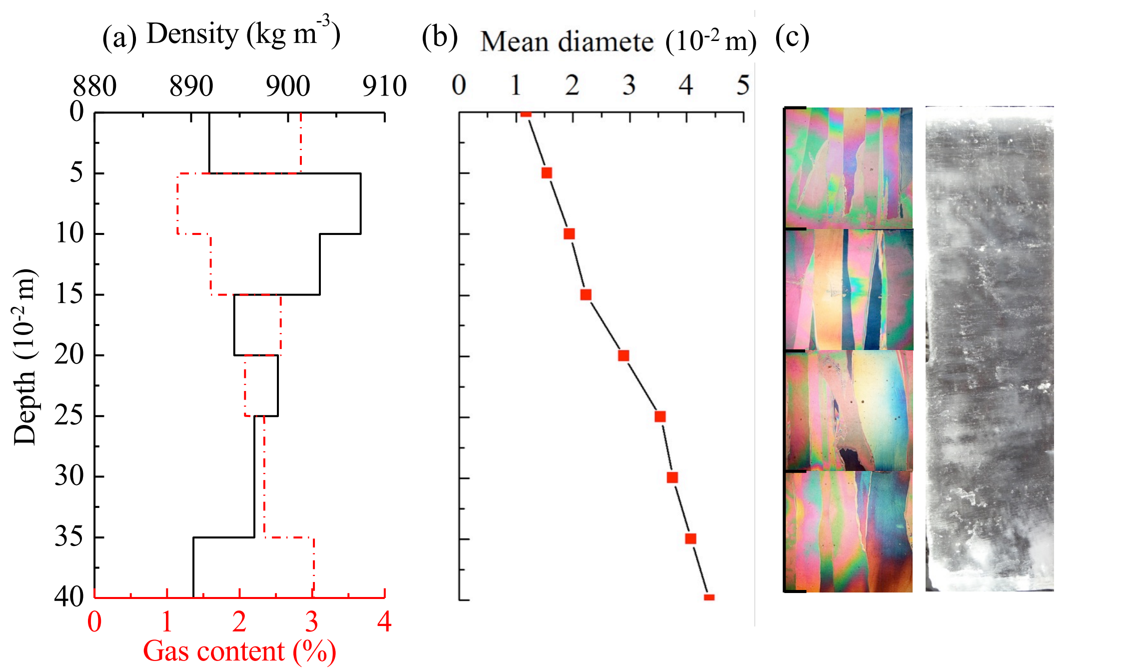

Fig. 5. (a) Vertical ice crystal structure under polarized light (left) and ice sample under normal light (right), (b) profile of the mean diameter of ice crystals in the horizontal plane and (c) profile of ice density and gas content.

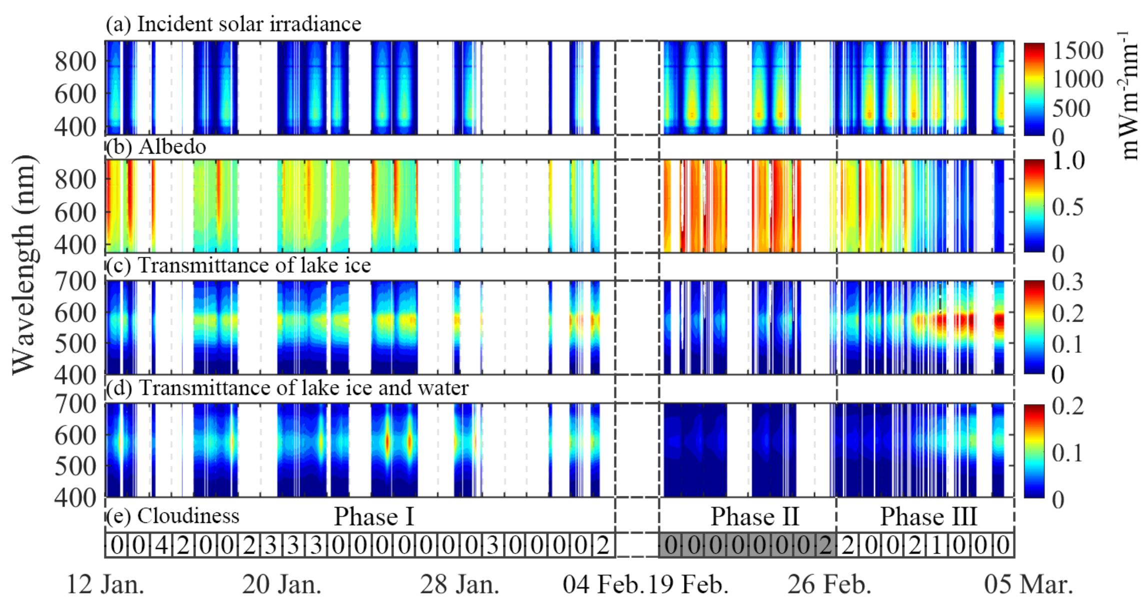

Fig. 6. Time series of (a) incident solar irradiance, (b) albedo, (c) transmittance of lake

ice, (d) transmittance of ice and a water layer beneath ice, and (e) cloudiness in tenths. The spectrum is shown for 8:00–18:00 each day. The white areas are missing data due to malfunction of Tribox3.

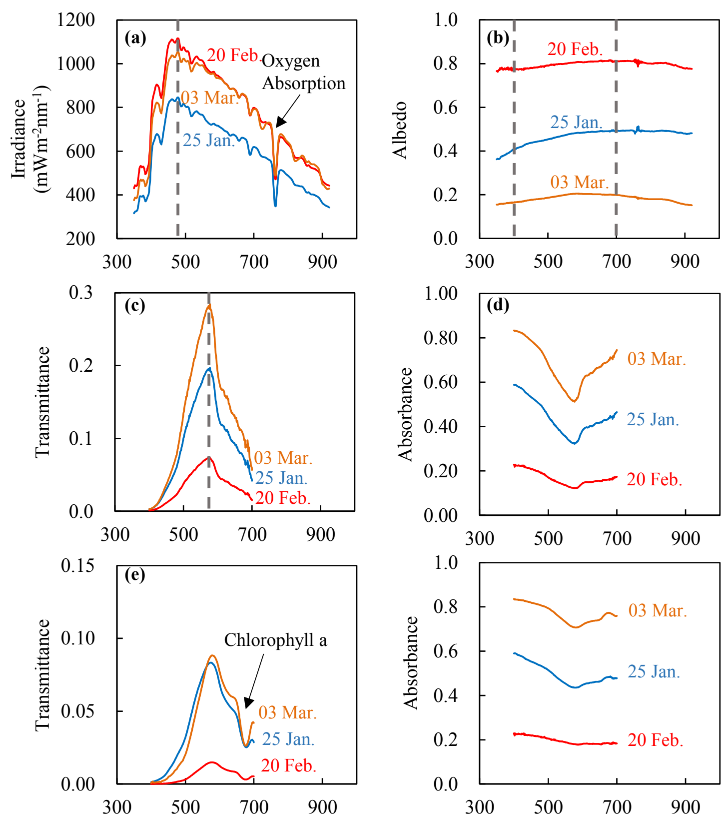

Fig. 7. The spectral results for three typical days in different phase at solar noon: 25 January (solar elevation SE = 30.3º), 20 February (SE = 38.3°), and 3 March (SE = 42.4º). (a) Incident solar irradiance, (b) Albedo, (c) Transmittance of ice, (d) Absorbance of ice, (e) Transmittance of ice and water, and (f) Absorbance of ice and water.

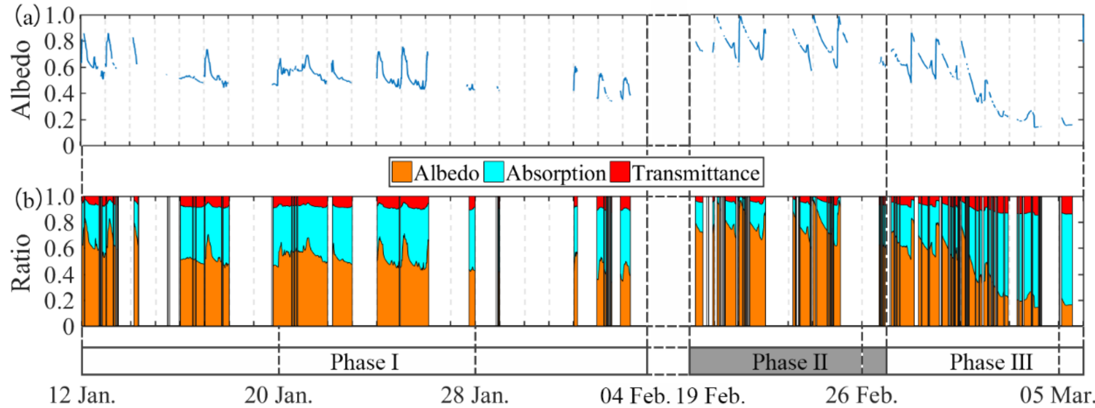

Fig. 8. (a) Broadband and PAR albedo. (b) PAR albedo and absorption and transmittance relative to the incident PAR irradiance.

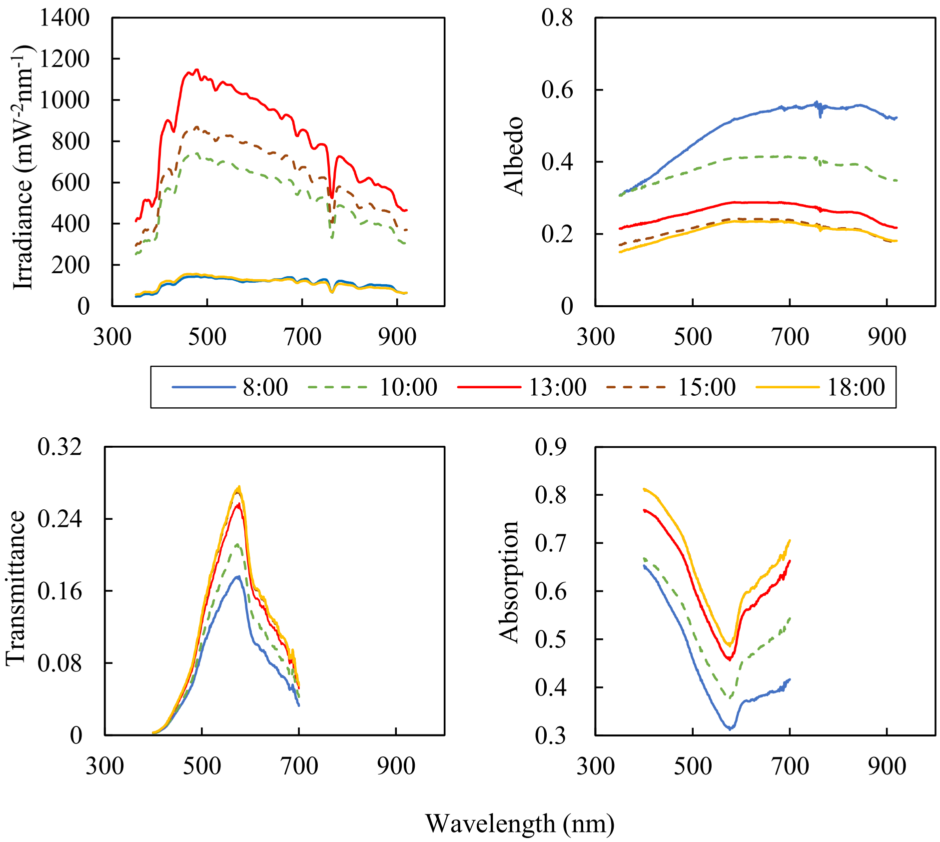

Fig. 9. Incident irradiance, albedo, transmittance and absorption of different hrs at 8, 10, 13, 15 and 18 hrs on 2 March. At the end points the solar elevation was about 10°. At 20 and 4 hrs and between the incident irradiance was zero.

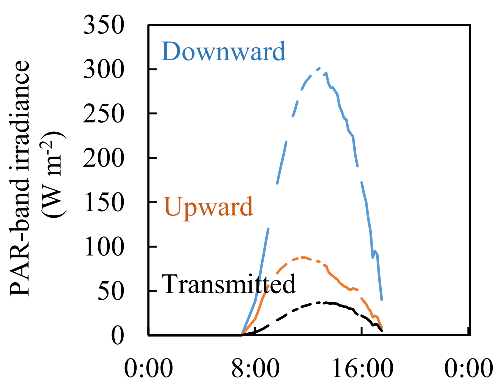

Fig. 10. Daily cycle of downward, upward and transmitted PAR irradiance on 2 March.

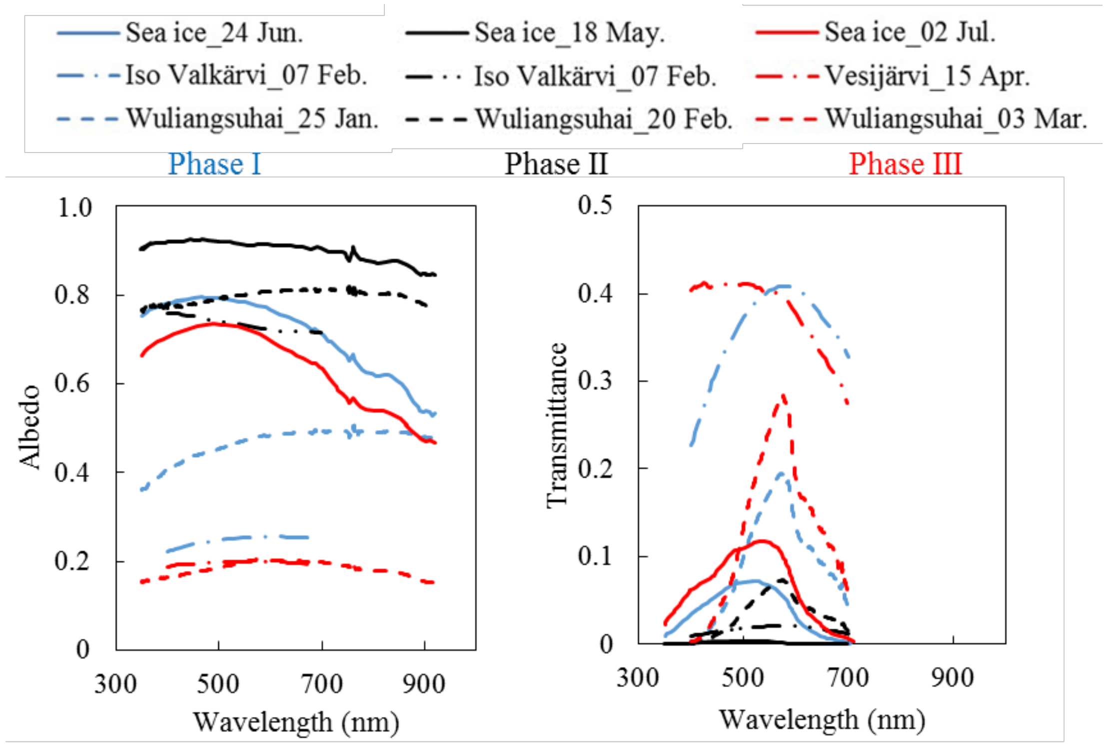

Fig. 11. The spectral albedo and transmittance of ice in lakes Wuliangsuhai, Iso Valkjärvi and Vesijärvi (Lei et al. 2011), and Arctic (Nicolaus et al. 2010b) in different phases (blue for phase I, black for phase II, and red for phase III).

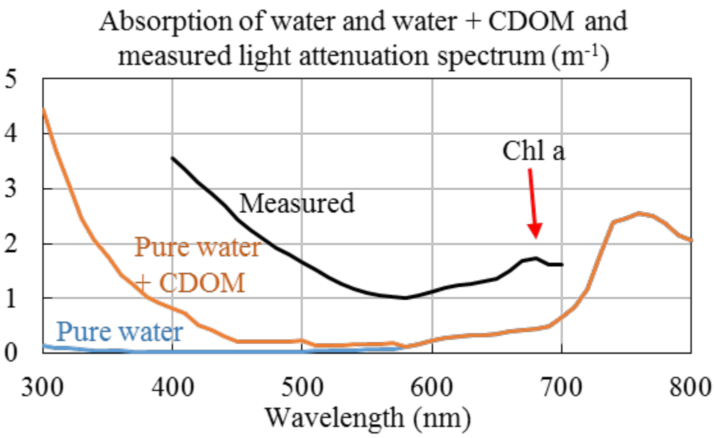

Fig. 12. Decomposition of light attenuation spectra for Lake Wuliangsuhai. Pure water shows standard pure water absorption curve (Smith and Baker, 1981), and CDOM was added based on the observed value of 0.004 m^{-1} (at 440 nm).

Online supplement:

Table A-1. Locations, times of observation, and ice and snow conditions at field sites of the comparative study. The data for Arctic sea ice were from Nicolaus et al, 2010b) and those on the lakes from Lei et al. (2011).

Phase	Date	Site	Location	Thickness (cm)		Mean water depth (m)
				Ice	Snow	
I	24/6/2007	Arctic sea ice	88° 10′ N 56° 40′ E	219.4	--	--
I	07/2/2009	Iso Valkjärvi	61° 11′ N 25° 06′ E	32.0	--	3.1
II	18/5/2007	Arctic sea ice	88° 20′ N 105° 00′ E	220.2	6.4	--
II	07/2/2009	Iso Valkjärvi	61° 11′ N 25° 06′ E	32.0	15.0	3.1
III	02/7/2007	Arctic sea ice	88° 10′ N 56° 40′ E	218.6	--	--
III	15/4/2009	Vesijärvi	60° 59′ N 25° 38′ E	34	--	6.0

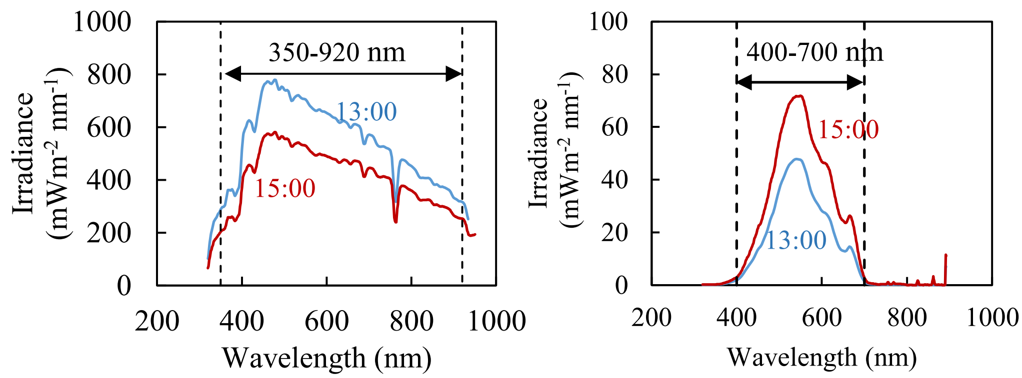

Fig. A-1. The incident (left) and transmitted (right) solar irradiance on 12 January. The lines show the limits of the band taken for the analyses (broadband, 350–920 nm, and PAR, 400–700 nm).

Fig. A-2. Ice surface conditions under the downward irradiance sensor (in the red square) on different dates in winter 2016.

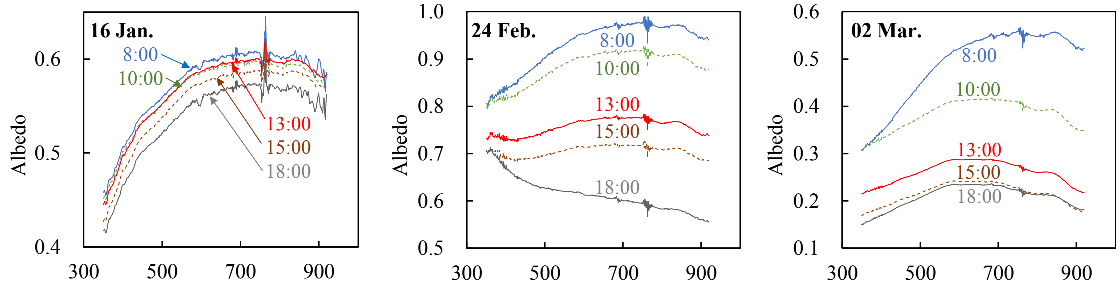

Fig. A-3. The diurnal cycle of the albedo in three phases and the solar noon was about 13:00.